the solid cannot attain its true equilibrium shape after transformation to the high-pressure phase. The bulk solid fragments into domains and the nanocrystal converts coherently from one shape to another. In the present case, nearly spherical nanocrystals with low-index surfaces convert to prolate ellipsoids with many high-index surfaces. This effect arises because the connectivity of the atoms cannot be altered. Burdett has shown that transition paths of this type can be viewed as three-dimensional Peierls distortions (*23*). This effect then explains the seemingly anomalous results that the rock salt–phase surface energy required to fit the nanocrystal size dependence of the phase transition was much larger than that expected for low-index rock salt–phase CdSe.

In the case of nanocrystals, where the surface energy makes a major contribution to the total free energy of the system, the transition path can actually determine the final state of the system. In a true equilibrium experiment, where path effects are not important, the rock salt surface energy would probably be less than that of the wurtzite, and a depression of the phase transition pressure would actually be observed. Thus, path effects play a major role in both the dynamics and the ultimate stable phases of nanometer-scale materials. Because of this, nanocrystals provide an opportunity to observe the effects of the transition path, which are masked in bulk systems. The potential is great for use of these and related experiments on nanocrystals to gain new understanding of the dynamics of solid-solid phase transformations in bulk systems.

Although these basic conclusions are general to wurtzite-phase nanocrystals, the specific surface energies reported here are probably influenced by the choice of surface ligand, 4-ethyl-pyridine. While the possibility does exist to actually change the ordering of wurtzite and rock salt surface energies through the use of an appropriate ligand, no significant changes in surface energy ordering are observed within the range of ligands we are currently able to use (Lewis bases). The question of surface modification aside, the present work demonstrates that a solid-solid phase transition smoothly evolves into a coherent molecular isomerization in finite size.

REFERENCES AND NOTES

1. A. N. Goldstein, C. M. Echer, A. P. Alivisatos, *Science* **256**, 1425 (1992).
2. C. J. Coombes, *J. Phys.* **2**, 441 (1972); P. Buffat and J.-P. Borel, *Phys. Rev. A* **13**, 2287 (1976).
3. The most obvious and striking example of this type of behavior is the fullerene cluster C_{60} [H. W. Kroto, J. R. Heath, S. C. O'Brein, R. F. Curl, R. E. Smalley, *Nature* **318**, 162 (1985)]. Metallic and ionic clusters are also expected to show this type of behavior [B. K. Teo, X. Shi, H. Zhang, *J. Am. Chem. Soc.* **113**, 4329 (1991); J. Deifenbach and T. P. Martin, *J. Chem. Phys.* **83**, 4585 (1985)].
4. C. B. Murray, D. J. Norris, M. G. Bawendi, *J. Am. Chem. Soc.* **115**, 8706 (1993).
5. J. E. Bowen Katari, V. L. Colvin, A. P. Alivisatos, *J. Phys. Chem.* **98**, 4109 (1994).
6. S. H. Tolbert and A. P. Alivisatos, in preparation.
7. For these experiments, we defined the thermodynamic phase transition pressure as the midpoint of the hysteresis curve, or equivalently, the average of the upstroke and downstroke transition pressures. This produces a bulk CdSe transition pressure of 2 GPa, in comparison with the upstroke value of 3 GPa. Experiments on bulk CdSe that show full hysteresis data include A. L. Edwards and H. G. Drickamer, *Phys. Rev.* **122**, 3196 (1962); A. Onodera, *Rev. Phys. Chem. Jpn* **39**, 65 (1969); and W. C. Yu and P. J. Gielisse, *Mater. Res. Bull.* **6**, 621 (1971).
8. M. Haase and A. P. Alivisatos, *J. Phys. Chem.* **96**, 6756 (1992).
9. X. S. Zhao, J. Schroeder, P. D. Persans, T. G. Bilodeau, *Phys. Rev. B* **43**, 12580 (1991).
10. S. H. Tolbert and A. P. Alivisatos, in *Nanophase Materials: Synthesis-Properties-Applications*, G. C. Hadjipanayis and R. W. Siegel, Eds. (NATO Advanced Study Institutes Series, Kluwer Academic, Dordrecht, Netherlands, 1993), pp. 471–482.
11. ———, *Z. Phys. D* **26**, 56 (1993).
12. A. P. Alivisatos, T. D. Harris, L. E. Brus, A. Jayaraman, *J. Chem. Phys.* **89**, 5979 (1988).
13. L. J. Cui, U. D. Venkateswaran, B. A. Weinstein, F. A. Chambers, *Phys. Rev. B* **45**, 9248 (1992).
14. J. D. Barnett, S. Block, G. J. Piermarini, *Rev. Sci. Instrum.* **44**, 1 (1973).
15. H. K. Mao and P. M. Bell, *Carnegie Inst. Washington Yearb.* **75**, 824 (1976).
16. A. N. Mariano and E. P. Warekois, *Science* **142**, 672 (1963).
17. Although either a mixture of pure zinc blende and pure wurtzite nanocrystals or nanocrystals of a mixed phase could produce the observed pattern, the observation of coherent transformations in this system argues in favor of the first option.
18. For a review of these ideas, see R. S. Berry, S. A. Rice, J. Ross, *Physical Chemistry* (Wiley, New York, 1980), pp. 875–883.
19. This value was obtained by fitting lattice contraction data versus nanocrystal size with the use of a simple Laplace law formalism (*6*).
20. B. N. Oshcherin, *Phys. Status Solidi A* **34**, K181 (1976).
21. R. E. Hanneman, M. D. Banus, H. C. Gatos, *J. Phys. Chem. Solids* **25**, 293 (1964).
22. U. D. Venkateswaran, L. J. Cui, B. A. Weinstein, F. A. Chambers, *Phys. Rev. B* **45**, 9237 (1992).
23. J. K. Burdett and T. J. McLarnan, *J. Chem. Phys.* **75**, 5765 (1981); J. K. Burdett, *Prog. Solid State Chem.* **15**, 173 (1984).

24. We thank M. Nicol, S. Mustonen, and A. Kadavanich for their technical assistance with this experiment. A.P.A. acknowledges an Alfred P. Sloan Foundation fellowship. This work has been partially supported by the donors of the Petroleum Research Fund, administered by the American Chemical Society, and by the Director, Office of Energy Research, Office of Basic Energy Sciences, Materials Science Division, of the U.S. Department of Energy (DOE) under contract DE-AC03-76SF0098. The experiments were performed using the facilities of the University of California–Lawrence Livermore National Lab Participating Research Team at the Stanford Synchrotron Radiation Laboratory, which is operated by the DOE, Division of Chemical Sciences.

24 February 1994; accepted 17 May 1994

First Principles Determination of the Effects of Phosphorus and Boron on Iron Grain Boundary Cohesion

Ruqian Wu, A. J. Freeman, G. B. Olson

Toward an electronic level understanding of intergranular embrittlement and its control in steels, the effects of phosphorus and boron impurities on the energy and electronic properties of both an iron grain boundary and its corresponding intergranular fracture surface are investigated by the local density full potential augmented plane wave method. When structural relaxations are taken into account, the calculated energy difference of phosphorus in the two environments is consistent with its measured embrittlement potency. In contrast to the nonhybridized interaction of iron and phosphorus, iron-boron hybridization permits covalent bonding normal to the boundary contributing to cohesion enhancement. Insights into bonding behavior offer the potential for new directions in alloy composition for improvement of grain boundary–sensitive properties.

The mechanical properties of ultrahigh-strength steels are often limited by the cohesion of crystal grain boundaries as influenced by the intergranular segregation of various metalloid impurities such as P and S. A thermodynamic theory developed by Rice and Wang (*1*, *2*) describes the mechanism of metalloid-induced intergranular embrittlement through the competition between plastic crack blunting and brittle boundary separation. While crystal plasticity considerations show interesting directional effects on the relative ease of crack tip blunting verified in critical bicrystal experiments, the most striking result of the analysis is the prediction that the potency of a segregating solute in reducing the "Griffith work" of brittle boundary separa-

R. Wu and A. J. Freeman, Department of Physics and Astronomy, Northwestern University, Evanston, IL 60208, USA.
G. B. Olson, Department of Materials Science and Engineering, Northwestern University, Evanston, IL 60208, USA.

tion is a linear function of the difference in segregation energy for that solute at a grain boundary (GB), ΔE_b, and at a free surface (FS), ΔE_s. Simply put, a solute with a positive energy difference $\Delta E_b - \Delta E_s$ (that is, ΔE_b is less negative) will be a more potent embrittler, or vice versa. The validity of this hypothesis has been supported experimentally for Fe-base materials for which significant data exist for both the relative embrittling potencies of solutes and the relevant surface thermodynamic quantities (*3*).

A predictive theory of intergranular cohesion can be developed by directly determining both ΔE_b and ΔE_s with present state-of-the-art energy band approaches; this offers the promise of major improvements in boundary cohesion-sensitive properties such as the stress corrosion resistance of ultrahigh-strength steels (*3*). To this end, we have carried out full potential linearized augmented plane wave (FLAPW) total energy calculations to investigate the effects of a P impurity in the FeΣ3[1$\bar{1}$0] (111) GB (*4*) and on the corresponding Fe(111) FS (*5*). In earlier calculations with a cell that contained only the first neighbor Fe atoms to the P impurity, we found that the Fe-P chemical interaction is slightly stronger at the Fe(111) FS because of a shorter interatomic distance. However, as a result of the small size of the unit cell and the exclusion of impurity-induced structural relaxation, the calculated $\Delta E_b - \Delta E_s$ was negative (−1.1 eV per cell), in contrast with the known embrittling potency of P in Fe.

In a subsequent calculation, we expanded the unit cell size for more realistic simulations (24 atoms per cell for the GB and 15 atoms per cell for the FS) (*6*). Using the equilibrium geometry determined from DMol cluster calculations (*7*), we found that structural relaxation may reduce the total energy of the clean FeΣ3[1$\bar{1}$0] (111) (the reference system for ΔE_b) by about 1.61 eV per cell. This reduction, in turn, results in a large correction to ΔE_b. By contrast, the impurity atoms do not induce significant reconstruction for the less constrained environment of the Fe(111) surface (*8*), and thus, ΔE_s is only slightly affected. As a result, $\Delta E_b - \Delta E_s$ becomes positive, 0.79 eV per P atom, in good agreement with experimental data. Here, we explore the mechanism of impurity-induced embrittlement more deeply by comparing the behaviors of P and B in the same FeΣ3[1$\bar{1}$0] (111) GB and Fe(111) FS environments. As B is known to be a GB cohesion enhancer in Fe (*1–3*), the comparison offers insights into the key electronic features underlying the influence of segregants on relative boundary cohesion.

We used a slab model (Fig. 1) to simulate both the P-Fe(111) FS and P-FeΣ3[1$\bar{1}$0] (111) GB, which minimizes GB interactions inherent in superlattice cells (*5*, *9*). For the B-Fe(111) and P-Fe(111) FS systems, the Fe(111) substrate is simulated by a 13-layer slab and the B and P adsorbates are placed pseudomorphically on the threefold hollow sites on both sides of the slab. For the GB systems, a 23-layer slab is adopted to simulate the clean FeΣ3[1$\bar{1}$0] (111). With 12 Fe layers in between, the interaction between the FS (introduced artificially in the slab model) and the GB is expected to be sufficiently reduced. The two-dimensional lattice constant and the unrelaxed Fe–Fe interatomic distance d are chosen from experimental values for bulk body-centered-cubic Fe: $d_{Fe-Fe} = 4.69$ atomic units. For the clean and impurity-adsorbed Fe(111) surface, the equilibrium atomic geometry is determined through FLAPW total energy minimization (*8*, *10*). For GB systems, geometries obtained from DMol cluster force calculations (*7*) are adopted. The GB structures are quite similar to those predicted with interatomic potentials based on the "embedded atom" method (*11*).

Although the impurity segregation energies as used by Rice and Wang are normally expressed relative to an impurity in dilute solution in crystalline Fe, the ΔE_b and ΔE_s computed here are referred to the calculated

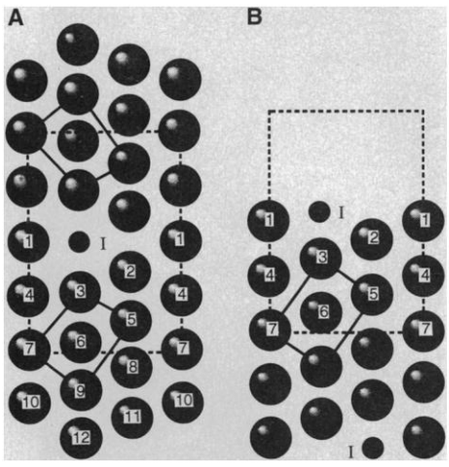

Fig. 1. Model and notation for the structure of Fe and impurities (I) at (**A**) Fe Σ3[1$\bar{1}$0] (111) grain boundary and (**B**) Fe(111) free surface. Solid rectangles correspond to unit cells of the body-centered-cubic structure. Dashed lines mark area mapped in Fig. 2.

Table 1. Calculated binding energies (in electron volts) of P and B in the Fe GB and FS environments and the decompositions into chemical, mechanical, and magnetic contributions. NM, nonmagnetic; FM, ferromagnetic.

	ΔE_b	ΔE_s	$\Delta E_b - \Delta E_s$	Δ Magnetic*
		P-Fe		
Unrelaxed (chemical)				
NM	−8.16	−7.58	−0.58	
FM	−8.19	−7.44	−0.75	−0.17
Relaxation (mechanical)				
NM	+2.19	+0.01	+2.18	
FM	+1.61	+0.07	+1.54	−0.64
Relaxed (total)				
NM	−5.97	−7.57	+1.60	
FM	−6.58	−7.37	+0.79	−0.81
		B-Fe		
Unrelaxed (chemical)				
NM	−8.27	−6.46	−1.81	
FM	−8.18	−6.67	−1.51	+0.30
Relaxation (mechanical)				
NM	+1.53	+0.10	+1.43	
FM	+1.69	+0.18	+1.51	+0.08
Relaxed (total)				
NM	−6.74	−6.36	−0.38	
FM	−6.49	−6.49	+0.00	+0.38

*Difference in $\Delta E_b - \Delta E_s$ between the NM and FM states.

Table 2. Calculated magnetic moments (in μ_B) in Fe. GB0 represents the relaxed clean Fe GB, and GB1 and GB2 denote the unrelaxed GB configurations for P and B, respectively.

Atom	Fe GB0	Fe GB1	P-Fe GB	Fe GB2	B-Fe GB	Fe(111)	P-Fe(111)	B-Fe(111)
Fe(1)	−1.28	2.40	1.40	2.50	2.05	2.71	1.74	2.33
Fe(2)	1.56	2.11	1.81	2.18	2.17	2.29	2.22	2.28
Fe(3)	1.43	1.81	1.49	2.07	1.90	2.36	1.73	1.71
Fe(4)	−1.75	1.81	2.01	1.86	2.15	2.20	2.30	2.31
Fe(5)	0.80	2.10	2.05	2.14	2.14	2.20	2.17	2.13
Fe(6)	1.42	1.85	1.98	1.85	2.02	2.11	2.27	2.29
Fe(7)	1.68	2.10	2.14	2.01	2.10	2.02	2.24	2.14

energy of an isolated two-dimensional monolayer with the same structure as the segregated monolayers of Fig. 1. The choice of segregation reference state does not matter to the calculation of the energy difference $\Delta E_b - \Delta E_s$ governing the impurity influence on GB cohesion.

In the FLAPW method, no shape approximations are made to the charge densities, potentials, and matrix elements. The core states are treated fully relativistically, and the valence states are treated semirelativistically (that is, without spin-orbit coupling). We used the Hedin and Lundqvist and the von Barth–Hedin formulas for the exchange-correlation potentials for the nonmagnetic and the spin-polarized calculations, respectively. Energy cutoffs of 150 and 950 eV were used for plane wave bases and star functions to describe the wave functions and the charge density and potential in the interstitial region, respectively. Within the muffin tin (MT) spheres ($r_{MT,Fe}$ = 2.0 au, $r_{MT,P}$ = 1.8 au, $r_{MT,B}$ = 1.3 au), lattice harmonics with angular momentum l up to 8 were adopted. Convergence was assumed when the average root-mean-square difference between the input and output charge (spin) densities was less than 5×10^{-4} e/au^3 (1×10^{-4} e/au^3), where e is the charge of an electron. The step-forward fixed-basis approach (*12*) was used to speed up the calculations conducted on a Cray-C90 supercomputer. Convergence for a given GB structure typically required 250 hours of computer time.

In previous calculations (*6*, *7*), we found that the clean FeΣ3[1$\bar{1}$0] (111) GB undergoes a phase transition to a hexagonal "ω phase" structure, which, in turn, results in an antiferromagnetic coupling in the core region of the GB. The segregated P atoms strongly push the Fe(3) atoms apart across the GB to form an "anti-ω" structure (Fig. 1), corresponding to a metastable state of the clean FeΣ3[1$\bar{1}$0] (111) GB. Such a large reconstruction gives a large "mechanical energy" contribution to the final value of ΔE_b (Table 1), adding 1.61 eV per cell. Physically, the mechanical energy is equal to the energy released during the relaxation of the clean Fe boundaries after impurity removal, and it is expressed as a positive number because the relaxed geometry corresponds to the lowest energy. The calculated Fe GB energy is 2.7 J/m^2 (or 2.4 eV per cell), compared with the calculated surface energy 3.4 J/m^2 (*10*). Both energies are somewhat large, but their difference (0.7 J/m^2) is in good agreement with experimental values.

Although the B impurity is considerably smaller than the P atom, it still cannot be well accommendated in the ω-Fe GB, and some B-induced Fe reconstruction should also be expected. Indeed, the calculated B–Fe(3) bond length is 4.06 au, only 9% shorter than that for P–Fe(3), 4.42 au. Surprisingly, this smaller relaxation gives rise to an even larger mechanical energy, 1.69 eV (Table 1), than that in the P-Fe case for which the Fe structure becomes closer to the metastable anti-ω phase structure.

The bond length is shorter in the FS environment than in the GB (*5*): The calculated $d_{P\text{-}Fe(3)}$ in P-Fe(111) is 4.5 au, and $d_{B\text{-}Fe(3)}$ in B-Fe(111) is 3.44 au. However, because the impurity atoms have a large space for adjustment in the vacuum region, the mechanical effects are expected to be less important in the FS environment. Indeed, the mechanical energy for the surface, ΔE_s, is usually less than 0.2 eV per cell (Table 1), even when the contributions from both the impurity relaxation and the impurity-induced Fe relaxation are considered (*6*).

We calculated the impurity-induced charge redistributions for the P-Fe(111) and B-Fe(111) FS systems by subtracting the superimposed charge density from a free P or B monolayer and a clean Fe(111) surface from the self-consistent charge density for the corresponding adsorption system (right column, Fig. 2). For P-Fe(111), strong charge accumulations are seen in the region between both

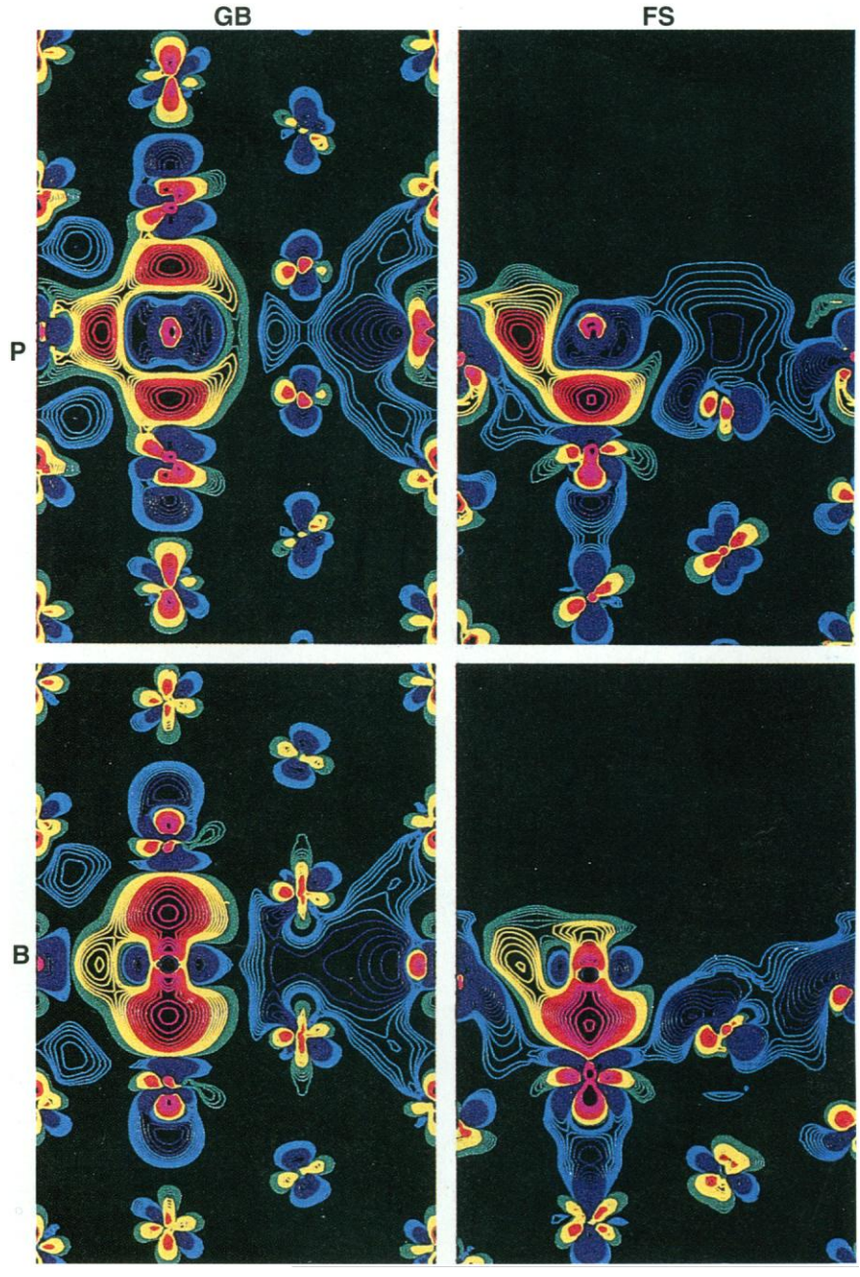

Fig. 2. The calculated valence charge density difference for P-Fe GB (top left), P-Fe(111) FS (top right), B-Fe GB (bottom left), and B-Fe(111) FS (bottom right). Contours start from 1×10^{-3} e/au^3 and increase successively by a factor of $2^{1/4}$; green, yellow, red, and pink denote charge accumulation and light and dark blue denote charge depletion. Regions displayed correspond to dashed cell of Fig. 1.

P-Fe(3) and P-Fe(1), indicating some chemical interaction between these atoms. The charge density at the inner region around the P atom is significantly decreased because of the effects of the surrounding Fe atoms. This apparent reverse charge transfer contradicts a simple estimate from the electronegativity (2.19 for P and 1.83 for Fe). These behaviors can be understood from the large spatial extension of the P 3*p* wave function and thus the "embedding" character of the P-Fe bonding (6).

By contrast, because the B 2*p* wave function is more localized than the P 3*p* wave function, the B-Fe(3) bonding is more covalent-like. In addition, B has only one 2*p* electron, whereas P possesses three 3*p* electrons. In the isolated monolayer geometry, the B 2*p* electron occupies the bonding p_{xy} states, which leaves the nonbonding p_z state empty. However, the p_z state becomes lower in energy by hybridizing with the Fe(3) d_{z^2} state, and thus, there is charge transfer from the in-plane p_{xy} states to the vertical p_z state (right bottom, Fig. 2). Therefore, B–Fe bonding shows much stronger spatial anisotropy compared to that between P–Fe (right top, Fig. 2), that is, stronger vertical B–Fe(3) bonding and weaker lateral B–Fe(1) bonding. As a result, the chemical part of ΔE_s for B in the FS environment, 6.67 eV per adatom, is 0.77 eV smaller than that for P.

The corresponding charge density differences were calculated for P-Fe and B-Fe GB systems (left column, Fig. 2). Because of the longer bond length, the charge accumulation and hence the strength of Fe-impurity bonding are weaker compared to the case in the FS environment. However, there are two P(B)–Fe(3) bonds across the GB, which results in a larger chemical energy in the GB systems by 0.75 eV for P and 1.51 eV for B. Although the B–Fe(1) interaction is much weaker than P–Fe(1), for the reason discussed above, the chemical energies for B and P in the GB environment become almost equal, 8.18 eV.

The presence of the impurity reduces the Fe(2)–Fe(2) interaction across the GB (Fig. 2) (*5*, *13*). The negative charge density difference can also be found above the Fe atoms in the FS environment (Fig. 2). This charge removal was once proposed to explain the embrittlement effect of impurities on GB cohesion (*13*). However, because this effect is even stronger for B, which is a known GB cohesion enhancer in Fe, the loss of charge does not appear to be an essential feature of embrittlement behavior.

The spin density difference contours for the P-Fe GB and P-Fe(111) FS are shown in the top panels of Fig. 3. As was revealed in the previous small cell calculations (5), the detrimental effects of the P impurities on the magnetization around the Fe(1), Fe(2), and Fe(3) atoms are very clear. Interestingly, P induces an enhancement of the magnetization around the second-rank Fe atoms that was not obtained in the previous calculations (5). This behavior is not seen in the charge density differences (Fig. 2), indicating that the P induces a short-ranged perturbation (screening) for the charge distribution but shows a long-ranged oscillatory behavior for the magnetic disturbance. In addition, the spin density around Fe(2) and Fe(1) is less affected in the FS environment, although the P–Fe(2) interatomic distances are smaller compared to those in the GB.

Quantitatively, the calculated magnetic moment in each Fe muffin-tin sphere is presented in Table 2. Referring to the unrelaxed GB configuration (GB1) corresponding to Fig. 3, the effects of P are obvious because it reduces the magnetic moment of Fe(1), Fe(2), and Fe(3) by 1.0 μ_B, 0.3 μ_B, and 0.32 μ_B, respectively, where μ_B is the Bohr magneton. At the FS, the reduction of the Fe(3) magnetic moment becomes as large as 0.63 μ_B. By comparison (bottom panels, Fig. 3), the effects of B on the magnetization of the surrounding Fe atoms are weaker, especially for the Fe(2) atom. Compared with the unre-

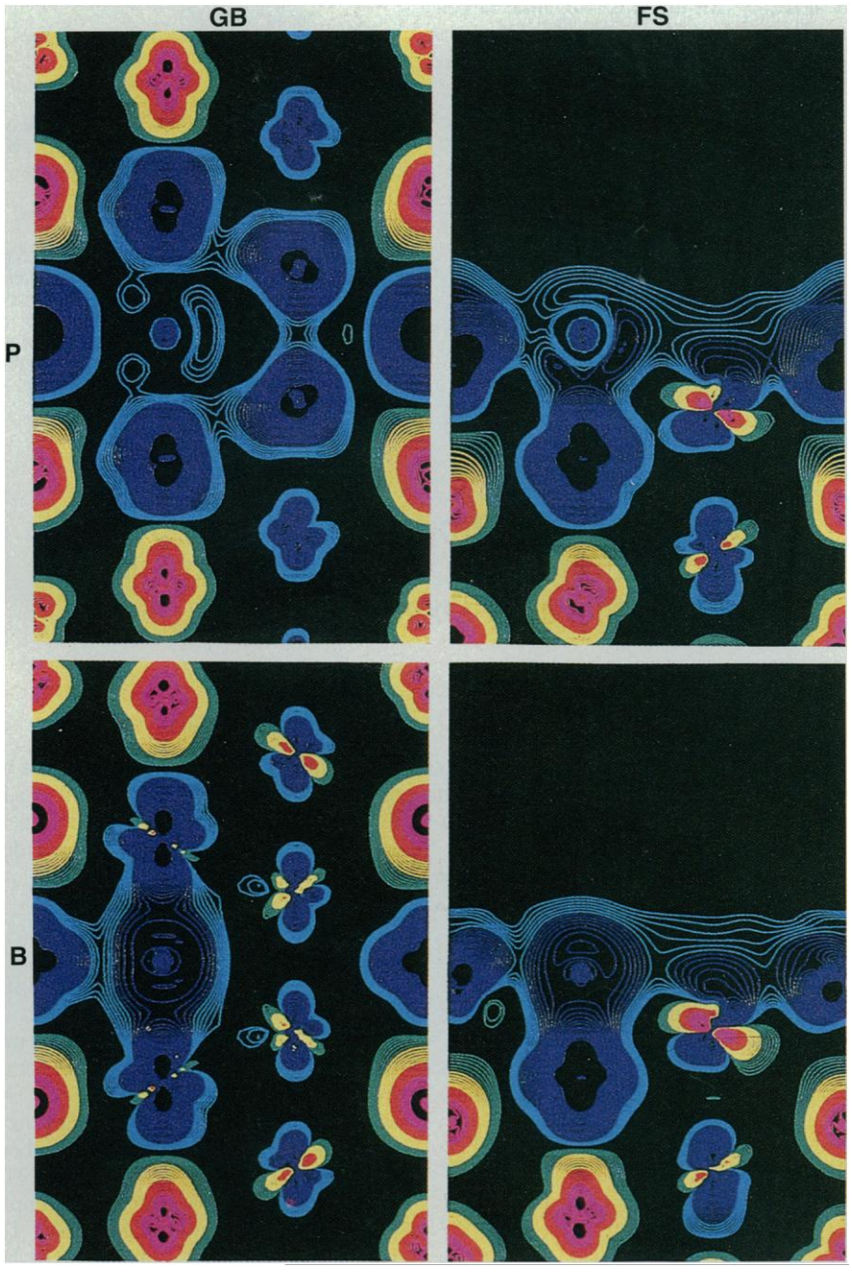

Fig. 3. The calculated spin-density difference for P-Fe GB (top left), P-Fe(111) FS (top right), B-Fe GB (bottom left), and B-Fe(111) FS (bottom right). Contours start from 1×10^{-3} *e*/au^3 and increase successively by a factor of $2^{1/4}$; green, yellow, red, and pink denote positive differences and light and dark blue denote negative differences.

laxed GB configuration (GB2), B reduces the magnetic moment of Fe(1), Fe(2), and Fe(3) by 0.45 μ_B, 0.01 μ_B, and 0.17 μ_B, respectively. The reduction of the Fe(3) magnetic moment in B-Fe(111), 0.65 μ_B, is even a little larger than that in P-Fe(111). The reduction of the Fe magnetization affects the segregation energy (Table 1, see the difference between results of ΔE for ferromagnetic and nonmagnetic states).

Finally, the calculated results for the $\Delta E_b - \Delta E_s$ difference controlling embrittlement are listed in Table 1. Because the impurity-induced structural relaxation is included, the segregation energy for P in the GB environment is smaller (less negative) than that on the FS; that is, $\Delta E_b - \Delta E_s = 0.79$ eV > 0, in good agreement with experiment (0.4 ± 0.2 eV per cell). According to the Rice-Wang thermodynamic theory (*1*), P is thus an embrittler for the FeΣ3[1$\bar{1}$0] (111) GB. By contrast, $\Delta E_b - \Delta E_s$ is almost zero (negative for the nonmagnetic case) for B, and thus, B is weakly cohesion enhancing.

Many factors affect the final results of $\Delta E_b - \Delta E_s$. The mechanical energy is especially important because the segregation energy differences are negative for both P and B when relaxation for the clean Fe GB is neglected. The magnetic energies are not large for either ΔE_b or ΔE_s separately (Table 1) but are indeed important for their difference. Therefore, a highly precise spin-polarized method and, importantly, equal treatment for the FS and GB systems are essential to obtain correct predictive results. The net magnetic contributions to the $\Delta E_b - \Delta E_s$ differences (Table 1) show that while magnetism reduces the embrittlement potency of P, it also reduces the cohesion enhancing effect of B.

As discussed earlier, impurity-induced reduction of Fe–Fe bonding is here eliminated as the mechanism for GB embrittlement by the comparison of P and B. Because the embrittlement behavior of an impurity is determined by $\Delta E_b - \Delta E_s$, it is essential to compare the difference of effects in the FS and GB systems. In both the FeΣ3[1$\bar{1}$0] (111) GB and the Fe(111) FS, there are three Fe(1) atoms. The strength of impurity-Fe(1) bonding (Fig. 2) does not change greatly from the GB to FS environments and thus is not significant for $\Delta E_b - \Delta E_s$. By contrast, impurity-Fe(3) bonding is expected to play the important role because one out of two of the vertical bonds in the GB is broken in the FS. Therefore, the spatial anisotropy of the bonding interaction between the impurity states with the surrounding Fe atom can be crucial to embrittlement behavior. Simply, impurities with stronger vertical and weaker lateral bonding are favorable to enhance the GB cohesion.

This conclusion is supported by the comparison of P and B. The B–Fe(3) bonding is much stronger than the B–Fe(1) bonding (bottom panels, Fig. 2); there is even a dangling bond above the B atom for B-Fe(111). Therefore, B prefers the GB environment to saturate the B–Fe(3) bonding. By contrast, P–Fe bonding is more embedded-like (electrostatic), and thus, there is no such dangling bond above P for P-Fe(111) (left top, Fig. 2). In addition, the P–Fe(1) bonding is almost as strong as that of P–Fe(3) bonding. Only one out of five P–Fe bonds in the GB is broken in the FS for P (one out of two for B), and thus, the reduction of the chemical energy for P is smaller than that for B. This is the main reason why the chemical part of $\Delta E_b - \Delta E_s$ for B is two times larger than that for P. Calculations for C and S impurities are in progress to verify the generality of these bonding trends, and further calculations will explore the interactions of impurity segregants and alloying elements. The fundamental insights developing from this research hold promise for new directions in alloy composition for enhancement of GB-sensitive properties.

REFERENCES AND NOTES

1. J. R. Rice and J.-S. Wang, *Mater. Sci. Eng. A* **107**, 23 (1989).
2. P. M. Anderson, J.-S. Wang, J. R. Rice, in *Innovations in Ultrahigh-Strength Steel Technology*, G. B. Olson, M. Azrin, E. S. Wright, Eds. (Proceedings of the 34th Sagamore Army Materials Research Conference, Government Printing Office, Washington, DC, 1990), p. 619.
3. G. B. Olson, *ibid.*, pp. 3–66.
4. In this notation, Σ3 refers to a special orientation relation between crystals for which one in three lattice points are coincident, [1$\bar{1}$0] denotes the crystal Miller indices of the axis of misorientation, and (111) denotes the habit plane of the boundary, both referred to the body-centered-cubic crystal lattice of Fe.
5. R.-q. Wu, A. J. Freeman, G. B. Olson, *J. Mater. Res.* **7**, 2403 (1992).
6. ———, *Phys. Rev. B*, in press.
7. S. P. Tang, A. J. Freeman, G. B. Olson, *ibid.* **47**, 2441 (1993).
8. R.-q. Wu, A. J. Freeman, G. B. Olson, *ibid.*, p. 6855.
9. G. L. Krasko and G. B. Olson, *Solid State Commun.* **76**, 247 (1990).
10. R.-q. Wu and A. J. Freeman, *Phys. Rev. B* **47**, 3904 (1993).
11. G. L. Krasko, in *Structure and Properties of Interfaces in Materials*, W. A. T. Clark, U. Dahmen, C. L. Briant, Eds. (MRS Symp. Proc. **238**, Materials Research Society, Pittsburgh, PA, 1991), pp. 481.
12. R.-q. Wu and A. J. Freeman, *Comput. Phys. Commun.* **76**, 58 (1993).
13. C. L. Briant and R. P. Messmer, *Philos. Mag. B* **42**, 569 (1980).

14. Supported by the Office of Naval Research (grant N00014-90-J-1363) with seed funding from the National Science Foundation (NSF) Materials Research Laboratory program (grant DMR88-16126) and a grant of Cray-C90 computer time at the NSF Pittsburgh Supercomputing Center from its Division of Advanced Scientific Computing.

8 February 1994; accepted 20 May 1994

Synthesis and Properties of a Cuprate Superconductor Containing Double Mercury-Oxygen Layers

P. G. Radaelli, M. Marezio, M. Perroux, S. de Brion, J. L. Tholence, Q. Huang, A. Santoro

A cuprate superconductor containing double mercury layers was synthesized with a high-pressure, high-temperature technique. The compound, with chemical formula $Hg_2Ba_2Y_{1-x}Ca_xCu_2O_{8-\delta}$, contains a double HgO layer with structure similar to that of rock salt. The prototype compound $Hg_2Ba_2YCu_2O_{8-\delta}$ is an insulator. Superconductivity is induced in the system by partially replacing yttrium with calcium.

All known copper-based superconductors have layered structures, where CuO_2 planes alternate with other structural elements. The compounds with the highest superconducting critical temperatures all contain, besides one or more CuO_2 planes, a single or double heavy metal–oxygen layer, like BiO, TlO, or HgO_δ. In the case of bismuth-based compounds, only structures containing double bismuth-oxygen layers have been synthesized (*1*). Thallium-containing superconductors can be formed with both a single and a double TlO layer (*2*, *3*). In 1993, a series of superconducting cuprates containing mercury was discovered. These compounds contain a single HgO_δ layer, where mercury is bonded with two oxygen atoms along the z axis, as in a dumbbell (*4*). However, double mercury layers are occasionally observed by electron imaging as

P. G. Radaelli and M. Perroux, Laboratoire de Cristallographie, CNRS/UJF, BP 166, 38042 Grenoble Cedex 09, France.
M. Marezio, Laboratoire de Cristallographie, CNRS/UJF, BP 166, 38042 Grenoble Cedex 09, France, and AT&T Bell Laboratories, Murray Hill, NJ 07974, USA.
S. de Brion and J. L. Tholence, Centre de Recherche sur les Très Basses Températures, CNRS/UJF, BP 166, 38042 Grenoble Cedex 09, France.
Q. Huang and A. Santoro, National Institute of Standards and Technology, Reactor Division, Gaithersburg, MD 20899, USA.